Chinese Chemical Letters 33 (2022) 4357–4362

Contents lists available at ScienceDirect

Chinese Chemical Letters

journal homepage: www.elsevier.com/locate/cclet

Urchin-like Nb_2O_5 hollow microspheres enabling efficient and selective photocatalytic C–C bond cleavage in lignin models under ambient conditions

Huan Chen[a,1], Donghui Hong[a,1], Kun Wan[a], Junjie Wang[a], Bo Niu[a], Yayun Zhang[a,*], Donghui Long[a,b,*]

[a] State Key Laboratory of Chemical Engineering, East China University of Science and Technology, Shanghai 200237, China
[b] Shanghai Key Laboratory of Multiphase Materials Chemical Engineering, East China University of Science and Technology, Shanghai 200237, China

ARTICLE INFO

Article history:
Received 22 September 2021
Revised 6 November 2021
Accepted 28 November 2021
Available online 3 December 2021

Keywords:
Niobium oxide
Urchin-like hierarchical structure
Photocatalysis
β-*O*-4 Lignin model
C_β radical

ABSTRACT

Selective cleavage of robust C–C bonds to harvest value-added aromatic oxygenates is an intriguing but challenging task in lignin depolymerization. Photocatalysis is a promising technology with the advantages of mild reaction conditions and strong sustainability. Herein, we show a novel urchin-like Nb_2O_5 hollow microsphere (U-Nb_2O_5 HM), prepared by one-pot hydrothermal method, are highly active and selective for $C_\alpha-C_\beta$ bond cleavage of lignin β-*O*-4 model compounds under mild conditions, achieving 94% substrate conversion and 96% C–C bond cleavage selectivity. Systematic experimental studies and density functional theory (DFT) calculations revealed that the superior performance of U-Nb_2O_5 HMs arises from more exposed active sites, more efficient free charge separation and the active (001) facet, which facilitates the activation of C_β–H bond of lignin models and generate key C_β radical intermediates by photogenerated holes, further inducing the $C_\alpha-C_\beta$ bond cleavage to produce aromatic oxygenates. This work could provide some suggestions for the fabrication of hierarchical photocatalysts in the lignin depolymerization system.

Lignin, the most abundant source of renewable aromatics in nature, holds great potential for the production of value-added chemicals, fuels, and functional materials as an alternative to fossil fuels [1–5]. However, its recalcitrant nature and structural complexity pose great technical challenges for the effective valorization of lignin [6]. One of the key issues in lignin depolymerization is the selective cleavage of C–O and C–C bonds [7], especially in the β-*O*-4 linkage which accounts for more than 50% of all interunit linkages [8]. Unfortunately, breaking the C–O bonds alone in lignin only yields no more than 50% of theoretical aromatic monomers [9]. Considering C–C backbone and oxygen-rich characters of lignin, C–C bond cleavage is a promising route to obtain valuable aromatic oxygenates. However, in contrast to the comprehensive development of C–O bond cleavage strategies, only a few examples shed light on the selective cleavage of lignin C–C bonds (β-*O*-4 and β-1 linkage), which may be due to the higher bond dissociation energy [10]. Conventional thermal catalytic processes, including pyrolysis, gasification, and noble metal-catalyzed hydrogenolysis, usually require hash reaction conditions (high temperature and pressure), and thus bond cleavage is nonselective, yielding a large number of low-functionalized by-products [11]. Thus, the development of a sustainable strategy for lignin depolymerization under mild conditions is highly attractive.

Photocatalysis is a promising technique for lignin conversion. The unique photogenerated reactive species can precisely cleave the targeted bonds in lignin while other fragile functional groups remain intact. In addition, mild conditions can inhibit undesired thermally induced side reactions, thereby preserving the aromatic rings [6,12]. A series of homogenous photocatalytic systems have been reported for lignin depolymerization with promising conversion and C–C bond cleavage selectivity, which can be attributed to the intimate contact between reactants and photocatalyst [13,14]. Homogeneous oxidation protocols for β-*O*-4 model compounds have been reported, mainly using vanadium (V)- [15,16], iridium (Ir)- [17], or cerium (Ce)-based [18] photocatalyst. However, the homogeneous nature of these transition metal-based catalytic system makes the catalyst separation and recovery challenging. There-

* Corresponding authors at: State Key Laboratory of Chemical Engineering, East China University of Science and Technology, Shanghai 200237, China.
E-mail addresses: yy.zhang@ecust.edu.cn (Y. Zhang), longdh@mail.ecust.edu.cn (D. Long).
[1] These authors contributed equally to this work.

https://doi.org/10.1016/j.cclet.2021.11.084
1001-8417/

fore, it is highly appealing to develop alternative strategies toward selective cleavage of C−C bond in lignin models using an active heterogeneous photocatalyst.

Niobium pentoxide (Nb_2O_5) has attracted intense attention in applications such as lithium-ion batteries, gas sensing, and microelectronics on account of its good thermal stability, high corrosion resistance, abundant surface properties, and superior optical properties [19,20]. In addition, Nb_2O_5 is also an n-type semiconductor with excellent photocatalytic properties, and thus has been extensively studied in light-driven environmental remediation, water splitting and some organic reactions [21]. Recently, Nb_2O_5 nanocrystals were reported to have shape-dependent photoactivities [22]. Therefore, various Nb_2O_5 multidimensional nanostructures, such as 3-dimentional (3D) nanospheres, 2D nanomeshes, and 1D nanorods, nanowires, and their 3D arrays have been rationally designed and fabricated to achieve efficient separation of photogenerated electron-hole pairs, which is deemed as a crucial factor in determining the photocatalytic performances [23,24]. Incidentally, to the best of our knowledge, there is no report on the application of Nb_2O_5 catalyst for photocatalytic cleavage of lignin C−C bonds. Herein, urchin-like 3D hierarchical Nb_2O_5 hollow microspheres (U-Nb_2O_5 HMs) were prepared by a hydrothermal method using resorcinol-formaldehyde (RF) resin as the template. Benefiting from the significantly improved charge separation efficiency and light utilization, the U-Nb_2O_5 HMs exhibited superior performance in the photocatalytic cleavage of C−C bonds in lignin models under light irradiation at room temperature. The morphology of U-Nb_2O_5 HMs was carefully examined by field-emission scanning electron microscopy (FESEM) and transmission electronic microscopy (TEM). X-ray photoelectron spectroscopy (XPS) and electron paramagnetic resonance (EPR) revealed the presence of oxygen vacancies in the U-Nb_2O_5 HMs. The experimental results and density functional theory (DFT) calculations showed that the (001) facet on the urchin-like Nb_2O_5 hollow microspheres offers enhanced activity in photocatalytic C−C bond cleavage. Finally, the reaction mechanism was revealed by radical trapping, isotope labeling, as well as DFT calculations. This work provides an effective strategy for the rational design and preparation of hollow metal oxide microsphere photocatalysts for efficient photocatalytic reactions.

The U-Nb_2O_5 HMs were prepared through a resorcinol-formaldehyde (RF) resin-assisted hydrothermal approach followed by removing the template through calcination (See in Supporting information). According to the thermogravimetric analysis (Fig. S1 in Supporting information), the content of Nb_2O_5 within the Nb_2O_5@RF polymeric microspheres was ~22.1%. The crystalline information of as-synthesized Nb_2O_5 photocatalyst was unveiled by X-ray diffraction (XRD) (Fig. 1a). Both U-Nb_2O_5 HMs and Nb_2O_5 exhibit a structural characteristic of a hexagonal Nb_2O_5 (TT-Nb_2O_5, JCPDS No. 07-0061) [22]. The diffraction peaks at 2θ of 22.6°, 28.6°, 36.7°, 46.2°, 50.7°, and 55.2° are assigned to the (001), (100), (101), (002), (110) and (102) plane, respectively.

Subsequently, field emission scanning electron microscopy (FESEM) and TEM were employed to observe the morphologies and structures of the resulting Nb_2O_5 samples. As shown in Fig. 1b, the low magnified FESEM images display a 3D hierarchical urchin-like microsphere structure with a diameter ranging from 2 μm to 4 μm, while the Nb_2O_5 is assembled by numerous nanoparticles (Fig. S2 in Supporting information). Individual broken microspheres show that the interior is empty (red dashed circle). It is worth mentioning that the urchin-like morphology is assembled by numerous nanorods protruding radially from the center in the high-magnification SEM images (Fig. 1c). This unique structure can offer a large specific area and uniformly dispersed active sites, thus increasing the contact area and enhancing the photoactivity. Additionally, energy-dispersive X-ray (EDX) analysis in Figs. 1f–i demonstrate that the element of niobium and oxygen were uniformly distributed within the U-Nb_2O_5 HMs. Similar to FESEM results, TEM images clearly show that the U-Nb_2O_5 HMs are composed of ultra-narrow nanorods and, more importantly, a hollow structure is confirmed (Fig. 1d). Many randomly selected nanorods in high resolution transmission electron microscopy (HRTEM) clearly showed standard lattice spacing of 0.385 nm, which was assigned to the (001) plane (Fig. 1e). Thus, the crystal growth of the nanorods seemed to follow the (001) zone direction, which is consistent with the XRD results.

The surface groups of the prepared sample were studied by fourier transform infrared spectroscopy (FT-IR). As shown in Fig. 2a, the intense broad band centered at around 655 cm^{-1} is assigned to the symmetric stretching vibration of Nb−O bond with a shoulder near 800 cm^{-1} [25]. Due to the similar atomic structures of the orthorhombic and hexagonal Nb_2O_5, the Raman spectra are also similar (Fig. 2b). The peaks between 200 and 360 cm^{-1} are characteristic of the bending modes of the Nb−O−Nb bonds. The region between 400 and 800 cm^{-1} refers to the symmetrical stretching of the Nb_2O_5 polyhedron. The main vibration at around 690 cm^{-1} is attributed to the vibration of weakly distorted NbO_6 octahedra [26].

The N_2 adsorption-desorption isotherms and Barrett-Joyner-Halenda (BJH) pore size analysis of as-synthesized samples are shown in Fig. S3 (Supporting information). Both samples exhibit the type IV isotherms with the H_3 hysteresis loop in the relative pressure (P/P_0) range from 0.4 to 1.0, which is typical for mesoporous materials. U-Nb_2O_5 HMs has a specific surface area (SSA) of 126.8 m^2/g with a total pore volume of 0.28 cm^3/g, obviously larger than that of Nb_2O_5 (Fig. S2a). The increased surface area was attributed to the protruding nanorods, which were conductive to the sufficient exposure of active sites during catalytic process. Furthermore, U-Nb_2O_5 HMs exhibited a multimodal pore-size distribution with smaller pores in the range of 2.3–12 nm and larger pores ranging from 12 nm to 80 nm (Fig. S2b). The smaller pores can be attributed to the spacing between the radially growing nanorods [27], while the larger pores may be due to the escape of CO_2 from the interior during the combustion of RF core.

Light absorption and utilization play an important role in photocatalytic reactions. Ultraviolet–visible diffuse reflectance spectrum (UV−vis DRS) was utilized to evaluate the optical properties of Nb_2O_5 catalysts. As shown in Fig. 2c, all samples exhibited strong absorption in the UV region. The bandgaps of U-Nb_2O_5 HMs and Nb_2O_5, were calculated to be 3.11 and 3.15 eV *via* Tauc plot, respectively. Thus, we can believe that the similar band structure of U-Nb_2O_5 and Nb_2O_5 contributes little to their photoactivity difference. However, thoroughly destroying the urchin-like hollow sphere structure by grinding decreased the conversion of PP-ol to 69% (Fig. S4 in Supporting information). This may be due to the fact that this hierarchical urchin-like hollow sphere structure allows multiple light reflections within the internal cavity [28,29] and multiple light-scattering among the nanorods (Scheme S1 in Supporting information) [30], allowing sufficient utilization of the light and thus promoting better photocatalytic performance.

The elemental composition of the catalyst and the valence state of the elements were investigated by XPS. The survey XPS spectrum in Fig. S5 (Supporting information) shows that, except for some residual carbon signal arising from adventitious carbon contamination, only Nb and O element were detected in all samples, suggesting the high purity of the catalysts. The three main peaks of the C 1s spectrum are centered at 284.7, 286.5, and 288.6 eV, corresponding to graphitic carbon (C−C), CH_x, and C−O=O, respectively (Fig. 3a) [31]. The high-resolution spectra of Nb 3d in all samples are dominated by two peaks at around 207.1 and 209.9 eV, corresponding to Nb $3d_{5/2}$ and Nb $3d_{3/2}$ (Fig. 3b), respectively [32]. The spin orbit separation was 2.8 eV, indicating that it exists mainly in

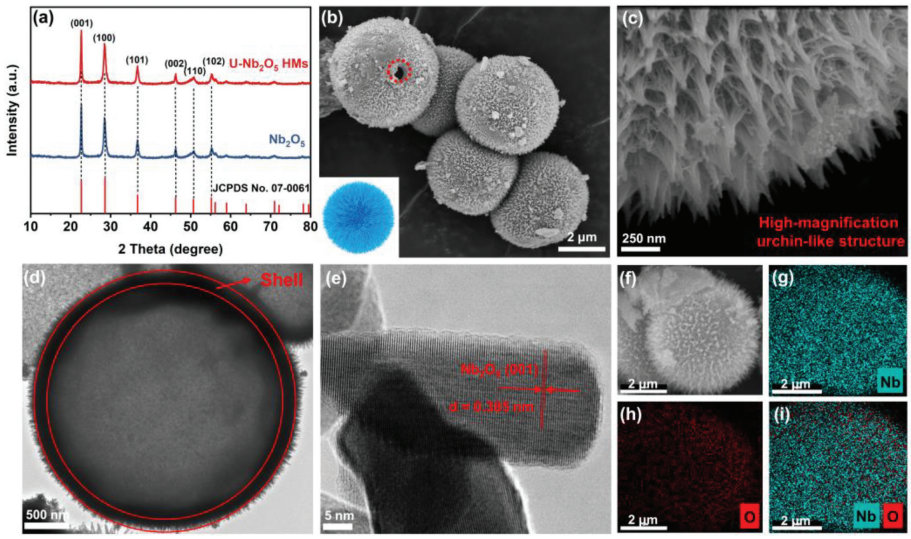

Fig. 1. (a) XRD patterns of U-Nb_2O_5 HMs and Nb_2O_5. (b) Low- and (c) high-magnification FESEM images of U-Nb_2O_5 HMs. (d) TEM and (e) HRTEM images of U-Nb_2O_5 HMs. (f-i) Elemental mapping of U-Nb_2O_5 HMs.

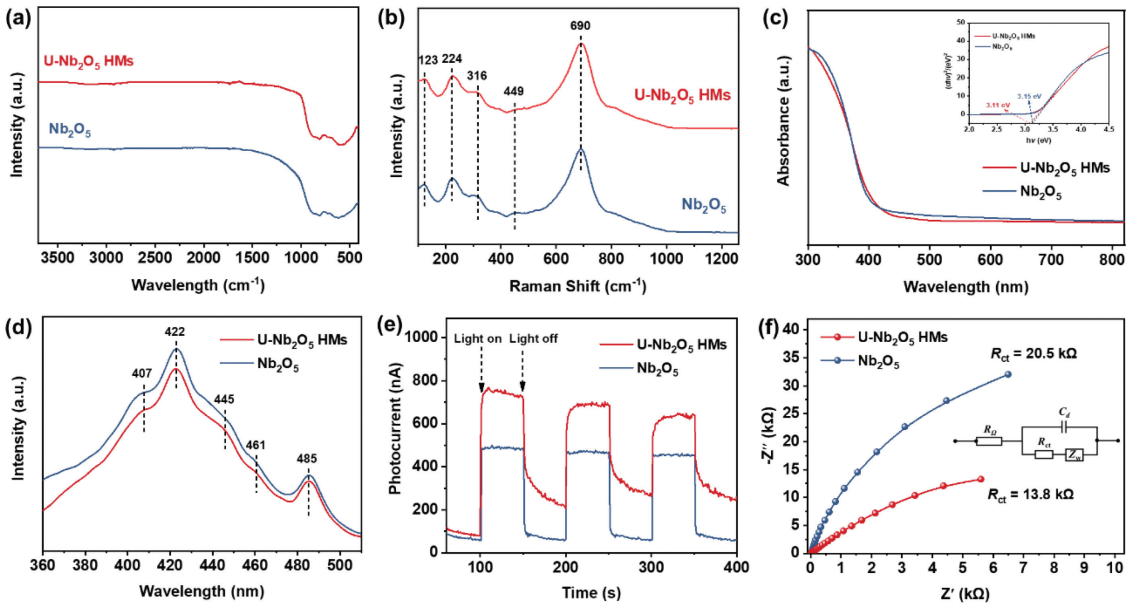

Fig. 2. (a) FT-IR spectra, (b) Raman spectra, (c) UV–vis spectra (inset Tauc plot), (d) PL spectra, (e) transient photocurrent response and (f) the electrochemical impedance spectra of U-Nb_2O_5 HMs and Nb_2O_5 (the equivalent circuit impedance model inset).

the Nb^{5+} state. However, the small characteristic peaks located at 205.9 and 208.8 eV were also observed and well corresponded to $3d_{5/2}$ and $3d_{3/2}$ peaks of Nb^{4+}, respectively [33–35]. The percentage of Nb^{4+} in U-Nb_2O_5 HMs was about 7%, which indicated that U-Nb_2O_5 HMs possess oxygen vacancies. It is widely accepted that surface oxygen species, especially surface oxygen vacancies, play an important role in oxidation reactions [36]. Thus, the relative content of surface oxygen vacancies in these two catalysts was analyzed by XPS spectra of O 1s. The high-resolution spectra of O 1s of all samples could be deconvoluted into two peaks (shown in Fig. 3c). The peak at 530.2 eV originated from the characteristic lattice oxygen bonding with niobium, while the peak located at 531.8 eV arose from surface adsorbed oxygen or oxygen vacancies [37]. As shown in Fig. 3c, U-Nb_2O_5 HMs displays a higher oxygen vacancy content (21.1%) than that of the Nb_2O_5 (12.6%). EPR measurement showed that all the sample exhibit the characteristic EPR signal at $g = 2.003$ (Fig. 3d), confirming the existence of oxygen vacancies [24]. Obviously, the peak intensity of U-Nb_2O_5 HMs is higher than that of Nb_2O_5. This is strongly consistent with the results of XPS.

On the other hand, photoelectrochemical techniques were employed to evaluate the transfer of photogenerated holes and electrons. Obviously, the photocurrent response of U-Nb_2O_5 HMs is notably stronger than that of Nb_2O_5 with several on/off transient photocurrent response under periodic irradiation of visible light (Fig. 2e), indicating a more efficient photogenerated electron-hole pair separation and transfer on the U-Nb_2O_5 HMs. Furthermore, electrochemical impedance spectroscopy (EIS) provides a powerful tool to study the charge transfer and recombination at semiconductor–electrolyte interfaces. Both Nyquist plots show explicit arcs, the radius of which is associated with the resistance of charge carrier transfer. It is evident that U-Nb_2O_5 HMs deliver a smaller arc, which verified that U-Nb_2O_5 HMs exhibit a more efficient interfacial charge transfer and more effective photogenerated electron-hole pair separation (Fig. 2f). We also measured

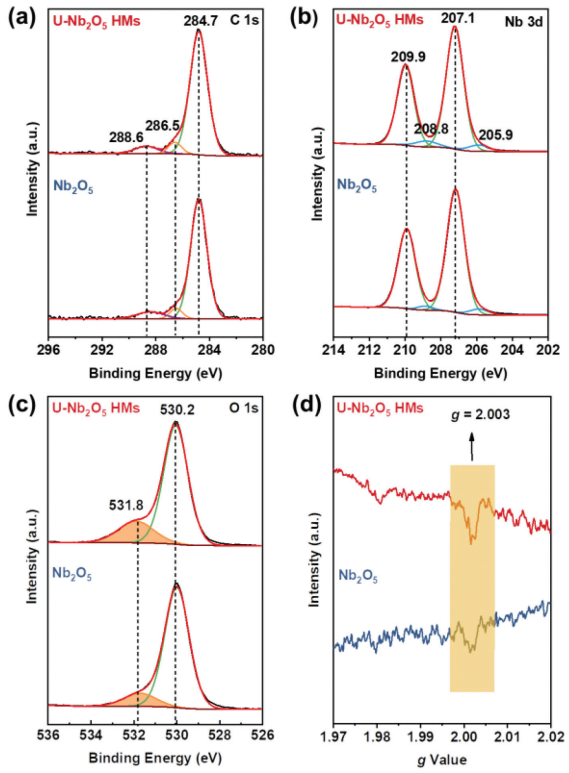

Fig. 3. XPS high resolution spectra of (a) C 1s, (b) Nb 3d, and (c) O 1s of U-Nb_2O_5 HMs and Nb_2O_5. (d) EPR spectra of U-Nb_2O_5 HMs and Nb_2O_5.

the photoluminescence (PL) spectra (excited at 285 nm) of two Nb_2O_5 photocatalysts to analyze the behavior of photogenerated holes and electrons since PL emission results from the recombination of charge carriers. As shown in Fig. 2d, the shapes of the PL emission spectra are similar, with several peaks at the same position. The first peak at around 407 nm (equivalent to 3.05 eV) is ascribed to the emission of band gap transition, and the energy of light approximately equally to the bandgap energy of U-Nb_2O_5 HMs photocatalyst (3.1 eV) [38]. The others should be attributed to the band edge free excitons, bound excitons, and surface defects [27,39,40]. Obviously, the PL intensity of U-Nb_2O_5 HMs is lower than that of Nb_2O_5, indicating that U-Nb_2O_5 HMs has a relatively lower electron-hole pair recombination rate, which favors higher photocatalytic activity.

To study the photocatalytic C–C bond cleavage regularity, a representative of lignin β-*O*-4 linkage, 2-phenoxyl-1-phenylethanol (PP-ol) with C_α–OH, C_α–C_β, and C_β–O bonds, was typically used as the substrate in this study. Results with different catalysts and reaction conditions are summarized in Table S1 (Supporting information). The reaction did not occur in the absence of catalyst (Table S1, entry 1). For Nb_2O_5, a modest activity with 55% conversion of PP-ol was detected (Table S1, entry 2). To our delight, U-Nb_2O_5 HMs confers remarkably higher photoactivity than Nb_2O_5, achieving a nearly completed conversion (94%) with a 96% of C–C cleavage selectivity (Table S1, entry 3), producing aromatic products including 2-phenoxylacetophenone (**2**), benzaldehyde (**3**), phenyl formate (**4**), and benzoic acid (**5**) (Figs. S6 and S7 in Supporting information). In addition, solvents play an important role in affecting catalytic performance and the product distribution. Among the three different solvents used, the highest photoactivity was obtained using acetonitrile, with a highest conversion of 94% and a 96% selectivity of C_α–C_β bond cleavage (Table S1, entry 3), probably due to the good solubility of PP-ol in CH_3CN. Acetone gave a medium conversion of 64% (Table S1, entry 6). In contrast, ethanol was the least suitable choice for this reaction with an unsatisfied conversion of 21% (Table S1, entry 7).

To elucidate the reaction mechanism, a series of control experiments were carried out. In the blank test, no target products were detected under dark condition, demonstrating the photocatalytic nature of this reaction (Table S1, entry 4). To identify the active species that involved in the reaction, the effects of trapping agents and reaction atmosphere and were explored. Isopropanol (IPA), *p*-benzoquinone (*p*-BQ), ethylenediaminetetraacetic acid disodium salt (EDTA-2Na) and $K_2S_2O_8$ were adopted as radical scavengers for hydroxyl radicals ($^{\bullet}OH$), superoxide anion radicals ($O_2^{\bullet-}$), photogenerated holes (h^+) and photoexcited electrons (e^-), respectively. As shown in Fig. S8 (Supporting information), addition of IPA, $K_2S_2O_8$ and *p*-BQ had little suppression on the conversion of PP-ol, suggesting that $^{\bullet}OH$, e^- and $O_2^{\bullet-}$ contribute little in this reaction. A significant decreased conversion was observed when the reaction atmosphere was changed to nitrogen (N_2), indicating that O_2 is indispensable and in this reaction (Table S1, entry 5). In comparison, addition of EDTA-2Na apparently inhibited the substrate conversion, revealing that h^+ is the main active species for the reaction.

Additional experiments were conducted to figure out the reaction intermediates. Benzaldehyde could be easily oxidized to benzoic acid (Scheme S2 in Supporting information, Eq. 1), which explained the presence of their mixture in the product. However, the ketone PP-one was hardly converted, together with low yields of target products under optimized condition, revealing that PP-one is not the intermediate for PP-ol conversion (Scheme S2, Eq. 3). This result is in direct contrast to those previously reported two-step photoredox strategy. Thus, a distinct one-step process may take place in our photocatalytic system. In some electrocatalytic systems, it is phenol rather than phenyl formate was detected as the product of C_α–C_β bond cleavage [41,42]. However, further studies with phenyl formate as the substrate demonstrate that it was relatively stable under reaction conditions without being hydrolyzed to phenol and HCOOH (Scheme S2, Eq. 2). Notably, the reaction was significantly inhibited when a radical scavenger, 2,2,6,6-tetramethyl-1-piperidinyloxy (TEMPO), was added into the reaction system, indicating that the reaction proceeds through a certain radical-catalyzed pathway (Scheme S2, Eq. 4).

For an in-depth understanding of the mechanism of the β-*O*-4 bond cleavage, especially to figure out whether the scission of C_α–C_β bond is catalyzed by the formation of C_α or C_β radical, kinetic isotope effect experiments with two deuterated substrates **1′–D** and **1″–D** were conducted (Scheme S3 in Supporting information). The conversion of **1′–D** with C_α–D was close to that of substrate of **1**, suggesting that the C_α–H oxidation is not the rate-determining step of C_α–C_β bond cleavage (Scheme S3, Eqs. 1 and 2). In contrast, the conversion of **1″–D** with C_β–D decreased significantly compared with that of **1**, indicating that the hydrogen abstraction of C_β–H is the rate-determining step (Scheme S3, Eq. 3). These results provide solid evidence of the formation of C_β radical as the reaction intermediate in C_α–C_β bond cleavage process.

On the basis of the above results and relevant literature reports [41–43], the possible mechanism of photocatalytic transformation of the lignin model compound over U-Nb_2O_5 HMs is proposed in Scheme S4 (Supporting information). Initially, photogenerated holes and electrons are produced in the valence band and conduction band under the irradiation of light. Subsequently, C_β radical is produced *via* C_β–H abstraction of lignin model compound by photogenerated holes. Lastly, the C_β radical reacts with O_2 and hydrogen to afford an unstable peroxide intermediate. The reaction is followed by the electron transfer in the peroxide intermediate through a six-membered ring transition state, inducing the cleavage of the C_α–C_β bond and the generation of benzaldehyde and phenyl formate. Benzoic acid is the product of overoxidation of

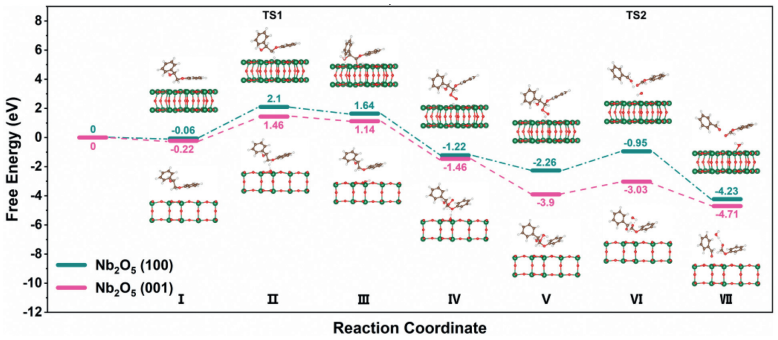

Fig. 4. DFT-calculated potential energy profiles and configuration diagrams of reactants, transition states, and products on the Nb_2O_5 (001) [pink] and Nb_2O_5 (100) [green] models.

benzaldehyde. On the other hand, the e^- in the conduction band of Nb_2O_5 may activate O_2 to form $O_2^{\bullet-}$, which subsequently deprotonate the benzyl alcohol toward alkoxide anion and finally result in the formation of by-product PP-one [43,44].

To further gain insight into the reaction intermediates and reaction pathways, DFT calculations were performed. The detailed elementary reaction steps and structures of $C_\alpha-C_\beta$ bond cleavage over Nb_2O_5 (001) and (100) models are shown in Fig. 4. Nb_2O_5 (001) displays a stronger adsorption capacity (−21.12 kJ/mol) (Fig. S9 in Supporting information) for PP-ol (step I) because unsaturated Nb^{5+} could enhance the adsorption of PP-ol. Then we simulate the adsorption of three possible radical intermediates, namely C_α radical, C_β radical, and oxygen radical, formed by the cleavage of $C_\alpha-H$, $C_\beta-H$, and O−H bonds, on (001) facet of U-Nb_2O_5 HMs, and find that C_β radical is the most stable form (Fig. S10 in Supporting information). This provides further evidence for the formation of the C_β radical as the reaction intermediate in our system.

It is widely accepted that the dehydrogenation of $C_\beta-H$ to form C_β radical is pivotal for $C_\alpha-C_\beta$ bond cleavage. Therefore, we calculated the corresponding energy barrier and reaction energy of this process on Nb_2O_5 (001) model with values of 1.68 and 1.36 eV, respectively (Steps II and III). The significant energy barrier and reaction energy confirm that the dehydrogenation of PP-ol to form C_β radical is the rate-determining step, and the apparent activation energy (G_{a1}) for (001) pathway was calculated to be 1.46 eV. In contrast, Nb_2O_5 (100) model exhibited a much higher energy barrier and reaction energy (2.16 and 1.7 eV, respectively) for this step, indicating that oxidation of $C_\beta-H$ on (100) facet is more difficult to occur. The apparent activation energy (G_{a2}) of (100) pathway was calculated to be 2.1 eV.

After the formation of C_β radicals, the reaction is followed by the combination with O_2 and hydrogen to give an unstable peroxide intermediate (steps IV and V). These two steps were calculated to be highly exothermic of −2.6 and −2.44 eV for Nb_2O_5 (001) model (−2.86 and −1.04 eV for Nb_2O_5 (100) model), respectively. The peroxide intermediate further undergoes a one-step $C_\alpha-C_\beta$ and O−O bond cleavage form benzaldehyde and phenyl formate (steps VI and VII). This step was calculated to be −0.81 eV, with a moderate energy barrier of 0.87 eV (−1.97 and 1.31 eV for Nb_2O_5 (100) model). By comparing reaction pathway on both Nb_2O_5 (001) and (100) facet, we conclude that the photocatalytic lignin $C_\alpha-C_\beta$ bond cleavage is much more favorable on (001) facet of U-Nb_2O_5 HMs.

After optimizing the reaction conditions, we then tested the generality of U-Nb_2O_5 HMs for photocatalytic depolymerization of other lignin models (Table S2 in Supporting information). Methoxy-substituted β-*O*-4 lignin models with −OMe either in the ketone part or phenol part were converted to aromatic oxygenates with 18%–48% yield.

For practical applications, the stability or reusability of a heterogeneous catalyst is crucial. In this study, the regeneration of U-Nb_2O_5 HMs was carried out by washing with absolute ethanol and acetonitrile three times after the photocatalytic reaction. The morphology and chemical structure of reused U-Nb_2O_5 HMs were confirmed by XRD, SEM, TEM, and XPS (Fig. S11 in Supporting information). After four consecutive reactions conducted under identical conditions, the photocatalytic activity of the U-Nb_2O_5 HMs had a slightly decrease (Fig. S12 in Supporting information). In addition, Moreover, a gram-scale reaction was conducted and achieve a moderate conversion (72%) of PP-ol after 24 h, underscoring the admirable scale tolerance of this photocatalytic system (Fig. S13 in Supporting information).

In summary, a novel urchin-like hierarchical Nb_2O_5 hollow microsphere was successfully prepared *via* a facile hydrothermal method, and subsequently used in the photocatalytic cleavage of $C_\alpha-C_\beta$ bond in lignin model compound. The results demonstrated that U-Nb_2O_5 HMs with active (001) facet showed high photocatalytic activity (94% of substrate conversion) and $C_\alpha-C_\beta$ bond cleavage selectivity (96%) simultaneously. Multicharacterizations revealed that the unique urchin-like hollow microsphere structure can expose more active sites and boost the separation of photogenerated electron-hole pairs, thereby enhancing the photoactivity. In addition, experimental studies coupled with DFT calculations suggested that the reaction proceeds *via* a key C_β radical intermediate which is more favorable on the active (001) facet.

Declaration of competing interest

The authors declare no conflicts of interests.

Acknowledgments

This work was financially supported by the National Natural Science Foundation of China (No. 22008073), and Shanghai Sailing Program (No. 20YF1410600). We want to thank Profs. Dongfang Niu and Yaqiao Liu for photoelectrochemical performance (PEC) measurement, Jianlei Yao for GC support, and Hongyu Zhang for picture drawing.

Supplementary materials

Supplementary material associated with this article can be found, in the online version, at doi:10.1016/j.cclet.2021.11.084.

References

[1] C. Xu, R.A. Arancon, J. Labidi, R. Luque , Chem. Soc. Rev. 43 (2014) 7485–7500.
[2] R. Rinaldi, R. Jastrzebski, M.T. Clough, et al., Angew. Chem. Int. Ed. 55 (2016) 8164–8215.

[3] Y. Zhou, Y. Qian, J. Wang, X. Qiu, H. Zeng, Biomacromolecules 21 (2020) 3231–3241.
[4] K. Chen, X. Qiu, D. Yang, Y. Qian, Green Chem. 22 (2020) 6357–6371.
[5] J. Wang, Y. Qian, L. Li, X. Qiu, ChemSusChem 13 (2020) 4420–4427.
[6] H. Chen, K. Wan, F. Zheng, et al., Renew. Sustain. Energy Rev. 147 (2021) 111217.
[7] C. Zhang, F. Wang, Acc. Chem. Res. 53 (2020) 470–484.
[8] M. Wang, F. Wang, Adv. Mater. 31 (2019) 1901866.
[9] M.V. Galkin, J.S. Samec, ChemSusChem 9 (2016) 1544–1558.
[10] X. Liu, F.P. Bouxin, J. Fan, et al., ChemSusChem 13 (2020) 4296–4317.
[11] C. Li, X. Zhao, A. Wang, G.W. Huber, T. Zhang, Chem. Rev. 115 (2015) 11559–11624.
[12] X. Wu, N. Luo, S. Xie, et al., Chem. Soc. Rev. 49 (2020) 6198–6223.
[13] P.J. Deuss, K. Barta, J.G. de Vries, Catal. Sci. Technol. 4 (2014) 1174–1196.
[14] P.J. Deuss, K. Barta, Coord. Chem. Rev. 306 (2016) 510–532.
[15] H. Liu, H. Li, N. Luo, F. Wang, ACS Catal. 10 (2019) 632–643.
[16] S. Gazi, W.K. Hung Ng, R. Ganguly, et al., Chem. Sci. 6 (2015) 7130–7142.
[17] Y. Wang, Y. Liu, J. He, Y. Zhang, Sci. Bull. 64 (2019) 1658–1666.
[18] Y. Wang, J. He, Y. Zhang, CCS Chem. 2 (2020) 107–117.
[19] R.A. Rani, A.S. Zoolfakar, J.Z. Ou, et al., Sens. Actuators B 176 (2013) 149–156.
[20] C.J. Zhang, S.J. Kim, M. Ghidiu, et al., Adv. Funct. Mater. 26 (2016) 4143–4151.
[21] K. Su, H. Liu, Z. Gao, P. Fornasiero, F. Wang, Adv. Sci. 8 (2021) 2003156.
[22] Y. Zhao, C. Eley, J. Hu, et al., Angew. Chem. Int. Ed. 51 (2012) 3846–3849.
[23] R. Song, H. Chi, Q. Ma, et al., J. Am. Chem. Soc. 143 (2021) 13664–13674.
[24] K. Su, H. Liu, B. Zeng, et al., ACS Catal. 10 (2019) 1324–1333.
[25] F. Hashemzadeh, A. Gaffarinejad, R. Rahimi, J. Hazard. Mater. 286 (2015) 64–74.
[26] H. Zhang, Q. Wu, C. Guo, Y. Wu, T. Wu, ACS Sustain. Chem. Eng. 5 (2017) 3517–3523.
[27] J. Chen, H. Wang, G. Huang, et al., J. Alloy. Compd. 728 (2017) 19–28.
[28] H. Li, Z. Bian, J. Zhu, et al., J. Am. Chem. Soc. 129 (2007) 8406–8407.
[29] J. Yu, H. Yu, H. Guo, M. Li, S. Mann, Small 4 (2008) 87–91.
[30] T. Xiong, F. Dong, Z. Wu, RSC Adv. 4 (2014) 56307–56312.
[31] T. Su, R. Peng, Z.D. Hood, et al., ChemSusChem 11 (2018) 688–699.
[32] Y. Wu, X. Fan, Y. Chen, et al., J. Mater. Chem. A 7 (2019) 20813–20823.
[33] S. Zhang, G. Liu, W. Qiao, J. Wang, L. Ling, J. Colloid Interface Sci. 562 (2020) 193–203.
[34] W. Zhao, W. Zhao, G. Zhu, et al., Dalton Trans. 45 (2016) 3888–3894.
[35] M. Li, X. He, Y. Zeng, et al., Chem. Sci. 6 (2015) 6799–6805.
[36] H. Yan, Q. Shen, Y. Sun, et al., ACS Catal. 11 (2021) 6371–6383.
[37] J. Chen, H. Wang, Z. Zhang, et al., J. Mater. Chem. A 7 (2019) 5493–5503.
[38] H. Cui, G. Zhu, Y. Xie, et al., J. Mater. Chem. A 3 (2015) 11830–11837.
[39] C. Yang, Z. Wang, T. Lin, et al., J. Am. Chem. Soc. 135 (2013) 17831–17838.
[40] G. Zhu, T. Lin, X. Lv, et al., J. Mater. Chem. A 1 (2013) 9650–9653.
[41] L. Ma, H. Zhou, X. Kong, Z. Li, H. Duan, ACS Sustain. Chem. Eng. 9 (2021) 1932–1940.
[42] T. Cui, L. Ma, S. Wang, et al., J. Am. Chem. Soc. 143 (2021) 9429–9439.
[43] H. Liu, H. Li, J. Lu, et al., ACS Catal. 8 (2018) 4761–4771.
[44] F. Su, S.C. Mathew, G. Lipner, et al., J. Am. Chem. Soc. 132 (2010) 16299–16301.